Multiplatform analysis of the radiative effects and heating rates for an intense dust storm on 21 June 2007

Aaron R. Naeger,[1] Sundar A. Christopher,[1,2] and Ben T. Johnson[3]

[1]   Dust radiative effects and atmospheric heating rates are investigated for a Saharan dust storm on 21 June 2007 using a combination of multiple satellite data sets and ground and aircraft observations as input into a delta-four stream radiative transfer model (RTM). This combines the strengths of the Cloud-Aerosol Lidar and Infrared Pathfinder Satellite Observations and CloudSat satellites and in situ aircraft data to characterize the vertical structure of the dust layers (5 km in height with optical depths between 1.5 and 2.0) and underlying low-level water clouds. These observations were used, along with Aerosol Robotic Network retrievals of aerosol optical properties, as input to the RTM to assess the surface, atmosphere, and top of atmosphere (TOA) shortwave aerosol radiative effects (SWAREs). Our results show that the dust TOA SWARE per unit aerosol optical depth was -56 W m^{-2} in cloud-free conditions over ocean and $+74$ W m^{-2} where the dust overlay low-level clouds, and show heating rates greater than 10 K/d. Additional case studies also confirm the results of the 21 June case. This study shows the importance of identifying clouds beneath dust as they can have a significant impact on the radiative effects of dust, and hence assessments of the role of dust aerosol on the energy budget and climate.

1. Introduction

[2]   Saharan dust aerosols can impact both shortwave (SW) and longwave (LW) radiation which can alter the global radiative budget and influence the climate. However, the dust aerosol effects on the climate are still not confidently understood due to the uncertainties in the dust optical properties particularly the single scatter albedo (ω_0) [*Forster et al.*, 2007]. The ω_0 can vary from moderately absorbing values near 0.92 to almost purely scattering values near 0.99 at a wavelength of 550 nm [e.g., *Haywood et al.*, 2011; *Johnson and Osborne*, 2011]. Thus, dust aerosols can reflect and absorb SW radiation in cloud-free conditions which is known as the SW direct radiative effect [*Haywood and Boucher*, 2000]. Dust particles with sizes on the order of several micrometers can also have a considerable impact in the LW by reducing the outgoing LW radiation at the TOA as the dust absorbs the radiation and emits at colder temperatures [*Zhang and Christopher*, 2003]. When the dust particles absorb the LW radiation, they also reemit a portion

of the radiation back toward the surface [*Yang et al.*, 2009]. The aerosol radiative effect can be quantified by calculating the radiative fluxes with or without aerosols. To reduce the uncertainties of the aerosol radiative effect, we must have a proper understanding of the aerosol optical properties and their vertical distribution especially when clouds are present [*Quijano et al.*, 2000]. For instance, the aerosol radiative effect can vary significantly over the ocean depending on whether or not water clouds reside beneath dust [*Quijano et al.*, 2000].

[3]   Observations from the Cloud-Aerosol Lidar and Infrared Pathfinder Satellite Observations (CALIPSO) have proved extremely valuable in understanding the vertical distribution of aerosols and clouds in the atmosphere [e.g., *Liu et al.*, 2008; *Chand et al.*, 2008; *Wilcox*, 2010]. Prior to the launch of CALIPSO, passive satellite remote sensing methods (e.g., Moderate Resolution Imaging Spectroradiometer (MODIS)) provided important information on the horizontal distribution of aerosols and clouds but with limited vertical information [*Qu et al.*, 2006]. Thus, the frequency of scenes consisting of aerosols residing among clouds in the same vertical column of air was unknown. Fortunately, CALIPSO observations have shown that scenes with aerosol above low-level water clouds are quite common especially in high aerosol loading regions [e.g., *Devasthale and Thomas*, 2011]. Therefore, single cloud and aerosol layers are less common than multiple cloud and aerosol layers in certain regions of the world which has significant implications in radiative transfer modeling.

[4]   Prior to the launch of the CALIPSO and CloudSat satellites, many studies were already using RTMs to analyze

---

[1]Department of Atmospheric Sciences, University of Alabama in Huntsville, Huntsville, Alabama, USA.
[2]Earth System Science Center, University of Alabama in Huntsville, Huntsville, Alabama, USA.
[3]Met Office, Exeter, UK.

Corresponding author: A. R. Naeger, Department of Atmospheric Sciences, University of Alabama in Huntsville, 320 Sparkman Dr., Huntsville, AL 35805, USA. (naeger@nsstc.uah.edu)
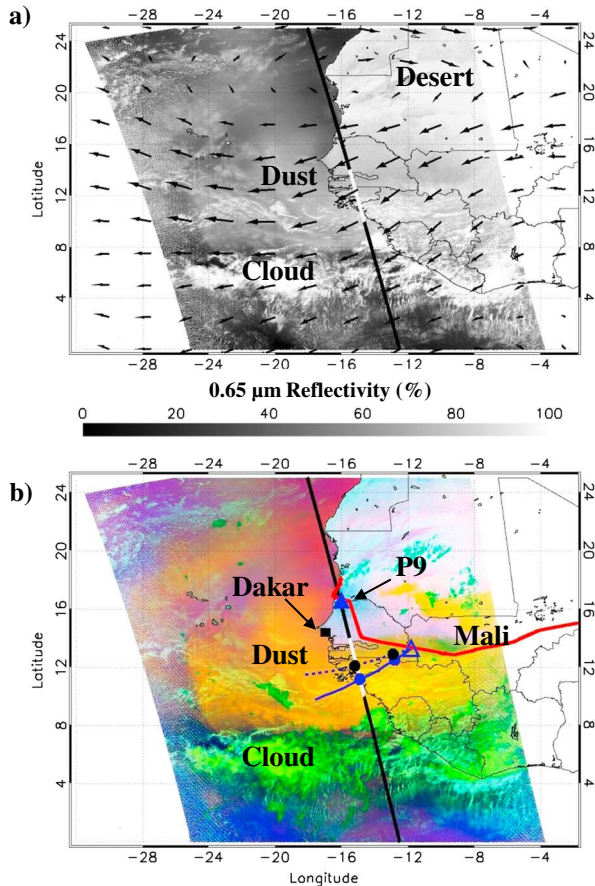
Figure 1. (a) MODIS 0.65 μm reflectivity image at approximately 1430 UTC on 21 June 2007 where the black line represents the CALIPSO transect as the satellite moves south to north on this day at approximately 1440 UTC. The white section of the CALIPSO transect shows the region of interest for this study (10°N–14°N). NCEP Reanalysis 700 hPa winds at 1200 UTC on this day are depicted by the black vectors. (b) MODIS red-green-blue (RGB) composite image at same time as in Figure 1a where the red channel is the BTD between the 12 and 11 μm bands, the green channel is the 0.65 μm band, and the blue channel is the BTD between the 11 and 8.5 μm bands. The red line depicts the BAE-146 flight path with the filled blue triangle showing the location of the P9 profile at 1402 UTC (16.6°N, 16.0°W) and the unfilled blue triangles showing the location of the P3-8 profile at about 1300 UTC (13.3°N, 11.8°W). The black square is the location of the Dakar AERONET station (14.4°N, 16.9°W). Forward trajectories from the HYSPLIT model computed by NCEP Reanalysis winds for an 11 h period beginning at the location of the P3-8 profile at 1300 UTC are shown by the blue lines where the solid and dashed lines depict the trajectory of the air at 3 km and 5 km, respectively. The filled circles along the blue lines show the trajectories after two hours and six hours into the HYSPLIT simulation initiated at 1300 UTC. The air in the vicinity of the P3-8 profile reached the CALIPSO transect at about 1900 UTC.

the top of the atmosphere (TOA), surface, and atmospheric radiative forcing and heating rates due to aerosols and clouds [e.g., *Quijano et al.*, 2000; *Zhang et al.*, 2004]. *Quijano et al.* [2000] conducted RTM simulations for theoretical cases

where dust aerosols resided above, between, or below clear and cloudy layers. They used theoretical case studies since spaceborne active lidars were not available for studying complex atmospheric vertical structures at the time of their study. *Zhang et al.* [2004] used data from the International Satellite Cloud Climatology Project and radiative transfer calculations to understand the Earth's radiation budget at the TOA, surface, and within the atmosphere. However, at the time, we had yet to observe the common situation of aerosols above clouds shown in *Chand et al.* [2008]. Now that active satellites are directly measuring the vertical structure of clouds and aerosols, we can use these observations to conduct calculations of radiative fluxes and heating rates in the atmosphere [*Huang et al.*, 2009].

[5] While TOA radiative effects can be assessed using broadband measurements from the Clouds and the Earth's Radiant Energy System [e.g., *Christopher and Zhang*, 2002; *Zhang and Christopher*, 2003], RTM simulations are needed to assess the impact of dust on the surface and atmosphere. Previous studies by *Huang et al.* [2009] simulated Taklimakan Desert dust storms using a delta-four stream RTM with CALIPSO observations as an input but they did not incorporate CloudSat data as they selected dust storm cases in cloud-free regions. In this study, we use the CALIPSO and CloudSat observations, and aircraft data from the GERBILS (Geostationary Earth Radiation Budget Intercomparisons of Longwave and Shortwave Radiation) campaign [*Haywood et al.*, 2011] to assess the vertical structure of a large dust plume with embedded low-level clouds over western Africa and the adjacent Atlantic Ocean on 21 June 2007. The GERBILS campaign consisted of 10 flights over North Africa and the Atlantic Coast from 18 to 29 June 2007. These data, along with Aerosol Robotic Network (AERONET) retrievals of aerosol optical properties, are used as inputs into a delta-four stream RTM [*Fu and Liou*, 1992]. The RTM is used to estimate the shortwave aerosol radiative effects (SWAREs) and radiative heating rates associated with the dust. The CALIPSO and CloudSat satellites transect crosses a range of land surface types and ocean enabling SWAREs and heating rates to be assessed for a wide range of surface albedos. We also present SWAREs and heating rates for two additional case studies involving low-level clouds beneath dust over the eastern Atlantic Ocean on 31 May and 18 June 2007.

2. Observations of the Dust Storm on 21 June 2007

2.1. MODIS

[6] The MODIS 0.65 μm reflectivity image at approximately 1430 UTC on 21 June 2007 shows higher reflecting clouds as indicated by the brighter white shades primarily south of 8°N while north of this boundary are mostly lower reflecting clouds and dust (Figure 1a). The MODIS red-green-blue (RGB) composite image at same time clearly depicts the intense dust storm (yellowish color) being transported from the Sahara Desert to the eastern Atlantic Ocean. Low-level clouds are also present among the thick dust storm from 10°N to 14°N along the CALIPSO transect as they appear in brighter shades of yellow within the yellow-orange belt of the dust storm.
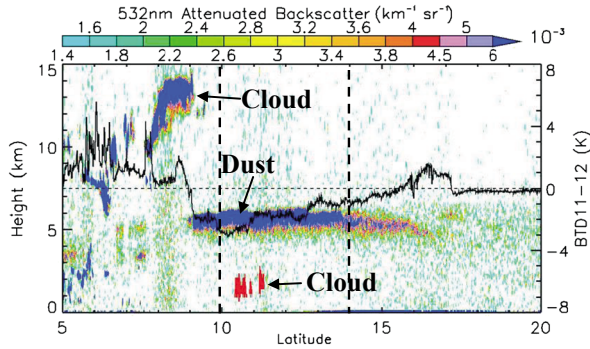
Figure 2. CALIPSO level 1B 532 nm total backscatter profiles during its transect in Figure 1 where the solid black line represents the MODIS brightness temperature differences between the 11 and 12 μm channels (BTD11-12) along this path. The location of low-level clouds beneath the dust storm (i.e., red markings) is identified using the CloudSat CPR cloud mask with a threshold of 20. The vertical dashed black lines demarcate the section of the transect from 10°N–14°N which is the focus of this study.

2.2. CALIPSO

[7] The Cloud-Aerosol Lidar with Orthogonal Polarization (CALIOP) instrument on board the CALIPSO satellite measures the vertical structure of the atmosphere by using backscattered light at 532 and 1064 nm [*Winker et al.*, 2003]. These measurements produce the level 1B product consisting of total backscatter (parallel plus perpendicular) at 532 and 1064 nm and perpendicular backscatter measurements at 532 nm for each 333 m footprint [*Powell et al.*, 2009]. *Rogers et al.* [2011] performed an extensive validation study on the CALIOP level 1B 532 nm total backscatter profiles and found that the daytime profiles agreed within 2.9% ± 3.9% with the suborbital NASA Langley airborne high spectral resolution lidar [*Hair et al.*, 2008]. The CALIPSO 532 nm total backscatter profiles during the transect on 21 June 2007 at about 1435 UTC reveal that the dust storm is elevated to about 5 to 6 km in height from 9°N to 17°N and is strongly scattering with backscatter values similar to the nearby clouds (Figure 2a). However, the 532 nm CALIOP signal is attenuated by the thick dust layer from 10°N to 14°N which means the sensor has difficulty detecting the low-level clouds along this section of the transect.

2.3. CloudSat

[8] CloudSat data have therefore been used to identify the low-level clouds in the CALIPSO transect. CloudSat flies about 20 s ahead of CALIPSO in the A-Train formation [*Stephens et al.*, 2002] and carries a 94 GHz millimeter wavelength cloud profiling radar (CPR) that easily penetrates through the dust layer [*Stephens et al.*, 2008]. Thus, we overlay the location of low-level clouds beneath the dust storm in Figure 3a by using the 2B-GEOPROF-LIDAR product that supplies a CPR cloud mask [*Mace et al.*, 2009]. We only show low-level clouds with cloud mask values >20 since false detection occurs only 5% of the time when using this threshold [*Mace et al.*, 2009]. CloudSat also combines their 2B-GEOPROF product with MODIS radiances to provide a 2B-TAU product [*Stephens et al.*, 2008]. This study uses

the cloud top and bottom heights in the GEOPROF-LIDAR product along with the cloud optical depth (COD) and cloud mean effective radius in the 2B-TAU product. The COD varied between about 6 and 18 for the low-level clouds with heights of 1 to 3 km from 10.4°N to 11.4°N for the 21 June case (Figure 3a). The mean effective radius of the clouds showed only slight variations between 10 and 15 μm.

2.4. BAE-146 Aircraft

[9] The GERBILS campaign consisted of Facility for Airborne Atmospheric Measurements (FAAM) BAE-146 aircraft flights that gathered in situ measurements of dust particle size, composition, and optical and radiative properties during June 2007 [*Johnson and Osborne*, 2011]. We focus on the B296 flight occurring on 21 June 2007 that departed from Niamey at approximately 1000 UTC and arrived at Nouakchott at approximately 1450 UTC. The BAE-146 aircraft flew directly through a portion of the intense dust
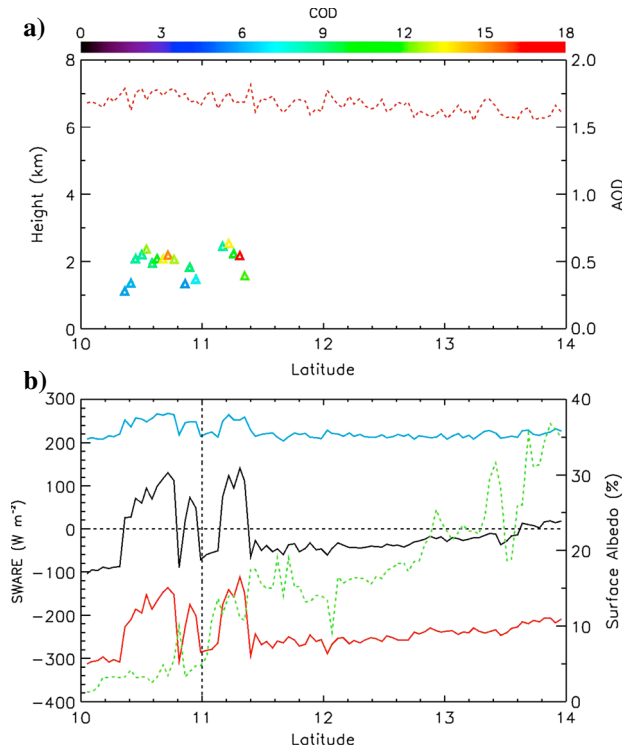

Figure 3. (a) CloudSat cloud top heights and COD are indicated by the colored triangles with their heights corresponding to height scale on the left *y* axis and their colors corresponding to the COD scale ranging from 0 to 18 at the top of the plot. AOD computed from the fitted CALIPSO extinction profiles along the transect is shown by the dashed red line with its corresponding scale ranging from 0 to 2 on the right *y* axis. (b) Instantaneous SWARE due to dust aerosols along the transect from 10°N–14°N on 21 June 2007 where the SWARE at the TOA, surface, and in the atmosphere is indicated by the solid black, red, and blue lines, respectively. The dashed vertical line at 11°N denotes the transition from ocean to land. The SWARE scale is on the left *y* axis of the plot while the computed albedo from the MODIS BRDF/Albedo Model Parameters product is shown in green with the scale on the right *y* axis.
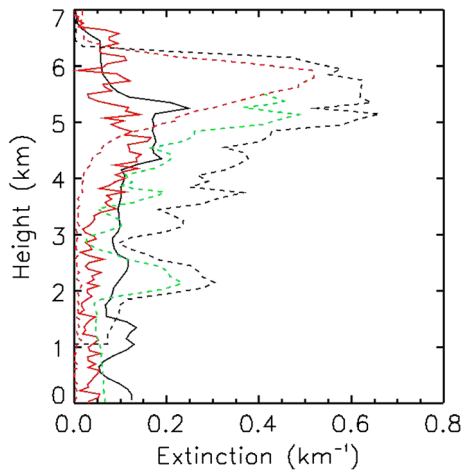
Figure 4. The 550 nm extinction profiles from the BAE-146 P3-8 and P9 profiles are shown by the dashed black and solid black lines, respectively. Original derived 532 nm extinction profiles using CALIPSO measurements averaged from 10°N to 14°N and 16.6°N to 16.75°N shown by the dashed red and solid red lines, respectively. The dashed green line shows the modified CALIPSO 532 nm mean extinction profile from 10°N to 14°N that is fitted to the structure of the BAE-146 P3-8 profile beneath 5.5 km in height.

storm observed by the MODIS sensor in Figure 1b. The unfilled blue triangle (13.3°N, 11.8°W) along the flight path identifies the location of the BAE-146 profile P3-8 occurring at about 1300 UTC. The 550 nm extinction coefficient profile derived during the P3-8 profile shows that the highest extinctions are in the middle atmosphere with values greater than 0.6 km^{-1} from 5 to 6 km in height (dashed black curve in Figure 4).

[10] The extinction profiles from the FAAM aircraft have an uncertainty of ±25% due to errors associated with the nephelometer and particle soot absorption photometer instruments [*Johnson and Osborne*, 2011]. Errors associated with inefficient sampling by inlets on the aircraft are an additional source of error that is not well constrained. Comparison of extinction profiles with Sun photometer estimates of AOD during DABEX [*Osborne et al.*, 2008] and GERBILS [*Johnson and Osborne*, 2011] show that on average, the aircraft overestimates AOD by about 20% in dust cases. Therefore, the aircraft extinction is more likely to be an overestimate than an underestimate (within the ±25% uncertainty). However, there is no clear basis for correcting this bias as the relationship of this bias to the sampling conditions or the properties of the dust is not well understood. By vertically integrating the extinction coefficient profile and taking into account the ±25% uncertainty, an AOD of 1.67 ± 0.42 at 550 nm was calculated for this P3-8 profile. Toward the end of the B296 flight, the BAE-146 measured the vertical profile of the atmosphere once again during its P9 profile occurring at approximately 16.6°N and 16°W from 1402 to 1422 UTC. As seen in Figure 1b the P9 profile flies through an atmosphere not nearly as dusty as the atmosphere measured during the P3-8 profile. Thus, the 550 nm extinction coefficients are much lower for the P9 profile (solid black curve in Figure 4) where the extinctions peak at about 0.2 km^{-1} near

5 km in height. An AOD of 0.70 ± 0.18 at 550 nm was calculated from the aircraft extinction profile of P9.

2.5. AERONET

[11] The AERONET consists of a network of Sun photometers across the globe used frequently for validating satellite retrievals [*Holben et al.*, 1998]. AERONET provides aerosol property retrievals from UV to near-IR wavelengths and we primarily take advantage of the ω_0 and asymmetry parameter (*g*) retrievals with uncertainties of approximately 0.03 and 3–5%, respectively [*Dubovik et al.*, 2000]. The *g* describes the proportion of the SW radiation that is scattered in the forward and backward directions where $g > 0$ indicates the radiation is scattered in the forward hemisphere and $g < 0$ indicates the radiation is scattered in the backward hemisphere. Since the *g* for Saharan dust aerosols is typically around 0.7 at 500 nm [*Formenti et al.*, 2000], they are strongly forward scattering aerosols which means that downward propagating radiation in the atmosphere will preferentially scatter in the hemisphere toward the surface when interacting with dust particles. The 21 June dust storm had moved over the Dakar AERONET station near the western African coast (i.e., Figure 1b) and aerosol retrievals were made at 1657 and 1724 UTC where the AOD at 675 nm was about 1.1. These retrievals showed an aerosol effective radius of approximately 1.1 μm and ω_0 values of 0.92, 0.98, 0.98, and 0.99 at 440, 675, 870, and 1018 nm. Thus, the dust storm is somewhat absorbing of visible radiation but very weakly absorbing of near-IR radiation. At these same four solar wavelengths, the Dakar station also retrieves *g* of 0.78, 0.74, 0.73, and 0.74, showing the forward scattering nature of the dust aerosols.

3. Radiative Transfer Modeling Methods

3.1. RTM

[12] The RTM used in this study is a delta-four stream model originally developed for calculating radiative fluxes in clear and cloud conditions [*Fu and Liou*, 1992, 1993] and later modified to account for aerosol radiative fluxes [*Rose and Charlock*, 2002]. It has six regular SW spectral bands from 0.2 to 4.0 μm and 12 longwave spectral bands between 2200 and 0 cm^{-1}. The RTM also contains spectral normalized extinction coefficients, single scatter albedos, and asymmetry factors for 25 different aerosol types. In this study, we assess the TOA, surface, and atmospheric radiative effects by taking the difference between the aerosol (i.e., dust) radiative fluxes and clear/cloud radiative fluxes from the RTM calculations.

3.2. Derivation of Aerosol Extinction Profiles From CALIPSO and Aircraft Data

[13] The first task we had in preparing the RTM for this 21 June 2007 dust storm simulation was to convert the CALIPSO level 1B 532 nm total backscatter profiles to extinction profiles by using a procedure similar to the one discussed in *Huang et al.* [2009]. We use the same equations (1)–(3) in *Huang et al.* [2009] to derive the extinction profiles but our procedure differs slightly. First, we apply a multiple scattering factor of 0.94 instead of 0.7 used in *Huang et al.* [2009] as *Liu et al.* [2011] conducted a detailed assessment

on the multiple scattering impacts on the CALIOP signal and found that the multiple scattering factor approaches 0.94 ± 0.015 when the extinction is smaller than 1 km^{-1}. Second, our study uses a single-scattering lidar ratio (i.e., extinction-to-backscatter ratio) of 55 sr which was found as the most appropriate lidar ratio after we compared the BAE-146 P9 550 nm extinction profile occurring from 1402 to 1422 UTC with nearby CALIPSO profiles of derived 532 nm extinction coefficients at approximately 1438 UTC on 21 June 2007. Our lidar ratio of 55 sr agrees with the average lidar ratio of 55.4 sr at 532 nm from 229 ground-based retrievals of Saharan dust conducted in *Schuster et al.* [2012]. When comparing the P9 and CALIPSO extinction profiles, we also found that using a lidar ratio of 55 sr throughout the entire CALIPSO profile can lead to overestimations in extinction within clean (i.e., aerosol-free) or relatively clean (i.e., background aerosol) layers. Therefore, we use a lidar ratio of 30 sr in the clean to relatively clean layers of the CALIPSO profile. *Tesche et al.* [2007] showed that areas of background aerosol conditions with very low AOD can be associated with lidar ratios of 25–30 sr. We locate clear, cloudy, and aerosol layers within the CALIPSO profiles through the level 2 (version 3) CALIOP product. The level 2 product is generated by identifying cloud and aerosol layers through applying a selective iterative boundary locator (SIBYL) algorithm on each level 1B profile and then a scene classification algorithm (SCA) determines whether the layer is cloud or aerosol [*Winker et al.*, 2009]. After applying these algorithms, the 5 km (level 2) product is created which consists of physical and optical properties of the cloud and aerosol layers [*Winker et al.*, 2009]. However, since the CALIPSO Cloud and Aerosol Discrimination (CAD) algorithm misclassified a significant portion of the dust storm as cloud, we use the BTD CAD algorithm [*Naeger et al.*, 2013] to properly identify the aerosols. This technique basically uses the negative MODIS BTD11-12 measured along the CALIPSO path (i.e., Figure 2a), since moderate to thick dust aerosols are typically associated with negative BTD11-12 [*Ackerman*, 1997; *Sokolik*, 2002; *Naeger et al.*, 2013], to convert any misclassified clouds in the profiles to aerosols.

[14] We show two 532 nm extinction coefficient profiles derived from this procedure in Figure 4 which are the mean profiles from 10°N to 14°N and 16.6°N to 16.75°N along the CALIPSO transect. The mean extinction profile from 16.6°N to 16.75°N (solid red line) is validated against the nearby BAE-146 P9 profile (solid black line), and they both exhibit extinction values around 0.15 to 0.2 km^{-1} between 4 and 5.5 km due to the presence of an elevated dust layer. The P9 profile exhibits an increase in extinction near 5.2 km to values greater than 0.2 km^{-1} that is not replicated in the CALIPSO profile. This difference may be caused by the fact that the aircraft profile occurs about 20 to 30 min prior to the CALIPSO overpass. In the lower atmosphere, the BAE-146 profile P9 shows several slight increases in extinction that are not shown by the CALIPSO profile, which is probably due to the CALIPSO lidar having already experienced some attenuation after passing through the midlevel aerosols that makes it difficult for it to detect these weak low-level aerosol layers. Then, we compare the CALIPSO-derived mean extinction profile from 10°N to 14°N (dashed red line) against the BAE-146 profile P3-8 (dashed black line). Even though the profile P3-8 occurs roughly 300 km

to the east of the CALIPSO transect, the National Centers for Environmental Prediction (NCEP) Reanalysis wind data reveal that the large-scale dynamics of the dust storm are similar in the east-west direction which suggests that this comparison is appropriate. Figure 1a shows the NCEP Reanalysis 700 hPa winds at 1200 UTC on 21 June (i.e., black vectors) where westerly winds with similar magnitude (e.g., length of the vector) and direction occur across most of the dust storm region. In fact, the wind magnitude and direction are nearly identical in the vicinities of the BAE-146 P3-8 profile and the CALIPSO transect from 10°N to 14°N. Besides the peak in extinction near the top of the dust layer at about 6 km, the mean extinction profile from 10°N to 14°N compares poorly to the BAE-146 profile P3-8 which is due to the very strong attenuation of the CALIPSO lidar in this optically thick dust layer. Below the top 1 km of the dust layer, the CALIPSO lidar is unable to detect the structure of the dusty atmosphere that is clearly shown by the profile P3-8. Due to the poor quality of the CALIPSO measurements beneath 5.5 km in this dust storm along 10°N–14°N, we fit the CALIPSO extinction profiles to the structure of the profile P3-8 (dashed green line in Figure 4).

[15] For this fitting procedure, we must first get the BAE-146 measurements onto the CALIPSO vertical height profile where we use linear interpolation as our BAE-146 and CALIPSO data have differing vertical resolutions of 100 and 30 m, respectively. Then, for each profile, we simply use the average of the CALIPSO extinctions from 5.5 to 6.0 km and add or subtract from this average based on the gradient of the BAE-146 extinction measurements below 5.5 km to calculate the fitted extinctions. Thus, the higher the CALIPSO-derived extinctions in the topmost layer of the dust, the higher the fitted extinctions below 5.5 km. In Figure 4, the large gradients in the BAE-146 extinction profile are reproduced in the fitted CALIPSO extinction profile, which shows significantly more structure to the dust storm than the original CALIPSO extinction profile (dashed red line). The lidar was finally able to penetrate through the dust layer during the 23 June transect at 1542 UTC where it identified some structure to the dust storm beneath the top layer (not shown). Although this transect was 2 days after our case study period, it still suggests that a significant amount of dust was most likely present below 5.5 km for our case study that was unable to be measured by the CALIPSO lidar. *Huang et al.* [2008] showed that when dust aerosols are lofted to the middle atmosphere, as with our case study, they can be transported long distances while maintaining a relatively consistent vertical structure along the path.

[16] To further assess the validity of using the BAE-146 aircraft profile extinction data, we simulate forward trajectories using the Hybrid Single Particle Lagrangian Integrated Trajectory Model (HYSPLIT) for an 11 h period on 21 June beginning at 1300 UTC at the location of the BAE-146 profile. These trajectories clearly show that the air at 3 and 5 km at the location of the BAE-146 profile was transported directly toward the region of the CALIPSO transect from 10°N to 14°N (Figure 1b). The air at the BAE-146 profile did not yet reach the CALIPSO transect that occurred at approximately 1440 UTC, but the air eventually did reach the transect at 1900 UTC (Figure 1b). Therefore, even though it is impossible to know the exact vertical structure of the dust storm in this study beneath 5.5 km along the CALIPSO

transect, the BAE-146 aircraft provides measurements close enough in time and space to help define the vertical structure. Also, note that the CALIPSO-derived profile and BAE-146 profile in Figure 4 both show high extinction values near 0.6 km^{-1} prior to the attenuation of the CALIPSO lidar beneath 5.5 km.

[17] After fitting the CALIPSO 532 nm extinction profiles from 10 °N to 14°N to the BAE-146 P3-8 profile, we input these profiles into the RTM SW band 1 (0.2–0.7 μm). Then, by using equation (4) in *Huang et al.* [2009], we are able to vary the extinction coefficient profiles for the remaining RTM bands according to the fitted CALIPSO 532 nm extinction coefficients in band 1 of the model.

3.3. Aerosol Optical Properties

[18] The optical properties of the aerosol, including the spectral variation of extinction are based on the 1.0 μm mineral dust aerosol type available in the RTM. This size class was chosen as the Dakar AERONET station retrieved an effective radius of approximately 1.1 μm for this dust storm [*Tegen and Lacis*, 1996]. However, other mineral dust sizes will be tested in the sensitivity analysis in section 4.3. After choosing this aerosol type, equation (4) in *Huang et al.* [2009] is used to compute extinction coefficients for the 5 remaining SW bands and 12 LW bands. To further reduce the dependence on the prescribed optical property values of the 1.0 μm mineral dust type in the model, we fit a polynomial curve to the ω_0 and g values retrieved at 440, 675, 870, and 1018 nm by the Dakar AERONET station and then compute a mean value of ω_0 and g for the RTM bands 1 (0.2–0.7 μm) and 2 (0.7–1.3 μm). From using this technique, we compute ω_0 of approximately 0.95 and 0.98 and g of approximately 0.76 and 0.74 for the RTM bands 1 and 2, respectively. These ω_0 values compare well to the data from the GERBILS campaign where the aircraft measured ω_0 at 0.55 μm from 0.92 to 0.99 with a mean of 0.97 [*Johnson and Osborne*, 2011]. Furthermore, the g values from this study are close to 0.73 found in *Johnson and Osborne* [2011] using T-Matrix calculations. Then, we use the prescribed ω_0 and g values of the 1.0 μm mineral dust type for the remainder of the SW and LW bands in the RTM.

3.4. Aerosol Optical Depth

[19] The AODs input into the RTM are taken from the fitted CALIPSO extinction profiles described above. The AOD is generally in the range of 1.6–2.0 from 10°N to 12°N and decreases to values between 1.5 and 1.7 northward of 12°N (Figure 3a). These values are remarkably similar to the AOD estimate of 1.7 at 550 nm from the BAE-146 profile P3-8 made at (13.3°N, 11.8°W) at around 1300 UTC which is not surprising since the CALIPSO extinction profiles were fitted to P3-8. It is difficult to compare our derived AOD to the MODIS Aqua overpass at about 1435 UTC on this same day since the MODIS AOD product shows significant cloud fractions (>25%) along much of the CALIPSO transect from 10°N to 13°N. However, from 13°N to 14°N, the MODIS AOD product shows cloud fractions mostly below 25% with AODs of 1.3 near 13°N decreasing to around 1.1 near 14°N. Thus, our AODs of 1.5 to 1.6 along this same section of the CALIPSO transect are higher than the AODs from the MODIS product which suggests our AOD derived from the fitted CALIPSO extinction profiles might be an overestimate.

The AOD retrieved at the Dakar AERONET station during the time of the CALIPSO overpass (1438 UTC) was around 1.1 at 675 nm but had peaked at 1.9 earlier in the day (~0920 UTC). This decrease occurred as the thickest regions of the dust storm, which this study is most interested in, had moved south of the Dakar station. For that reason, the AOD from Dakar is not used as a constraint for the RTM simulation but is simply noted here for comparison.

3.5. Spectral Surface Albedo

[20] Another critical input that must be addressed is the spectral albedos from the MODIS BRDF/Albedo Model Parameters product (MCD43C1). The Bidirectional Reflectance Distribution Function (BRDF) model parameters in the MCD43C1 product allows us to compute albedos that are appropriate for this particular case study by using the solar zenith angles on this day which is described in *Schaaf et al.* [2002]. The MCD43C1 product contains a visible broadband channel from 0.3 to 0.7 μm that we use to compute an albedo for the RTM band 1 (0.2–0.7 μm). It also contains BRDF model parameters for the seven MODIS solar bands which we use to compute an albedo for the SW RTM bands 2–4. MODIS bands 2 (0.85 μm) and 5 (1.2 μm) are used to compute an albedo for the RTM band 2 (0.7–1.3 μm). Then, MODIS bands 6 (1.6 μm) and 7 (2.1 μm) are used to compute an albedo for the RTM bands 3 (1.3–1.9 μm) and 4 (1.9–2.5 μm), respectively. Due to the lack of albedo information for input into the RTM bands 5 (2.5–3.5 μm) and 6 (3.5–4.0 μm), we simply set bands 5 and 6 to the band 4 albedo. It is difficult to obtain albedo information for bands 5 and 6 due to the very small amount of solar energy that exists at these wavelengths as about 99% of the solar radiation is confined to the wavelength range of 0.3–3.0 μm. Therefore, our approach of using the band 4 albedo for the bands 5 and 6 albedos will cause insignificant uncertainties in our RTM simulations. The solar zenith angle (SZA) is an important input into the RTM and the SZA decreased from 26.7° to 24.2° between 10°N and 14°N along the CALIPSO transect in Figure 2a.

3.6. Cloud and Meteorological Variables

[21] The cloud top and base heights along with COD and mean effective radius retrieved by the CloudSat satellite from 10°N to 14°N are input into the model. However, we use the CloudSat cloud mask values, which range from 0 to 40, to ensure that only clouds detected with high confidence are input into the model. A high confident detection occurs when the cloud is given a cloud mask value of at least 20 [*Mace et al.*, 2009]. Finally, Global Forecast System (GFS) 1° by 1° atmospheric profiles of temperature and specific humidity are used as inputs into the RTM.

4. RTM Results and Discussion

4.1. SWARE

[22] In this study, we chose cases where dust was observed above water clouds. The SWARE due to dust aerosols is computed by simulating the RTM with dust and clouds and then performing another simulation with only clouds. The difference between the radiative flux of dust and cloud ($F_{dust+cloud}$) and the radiative flux of cloud only (F_{cloud}) gives the instantaneous SWARE due to dust alone which is shown

for the 21 June 2007 dust storm in Figure 3b. The surface albedo in Figure 3b (dashed green line) is the solar broadband albedo (0.2–4.0 μm) computed by taking the mean over the SW RTM bands 1–6. Between about 10°N and 11°N, the SW broadband albedo is less than 5% since the CALIPSO transect is still over water. Around 11°N, the transect is over land where albedos generally increase reaching maximum values of around 35% near 14°N. The increase in surface albedo to 10% around 10.8°N is caused by a brief CALIPSO transect over a coastal land area before emerging over ocean once again until the primary land mass is encountered at 11°N.

[23] Over the cloud-free water background (10°N–10.3°N) the SZA is about 26.7° resulting in 1226 W m^{-2} of solar radiation available at the TOA. The dusty atmosphere reflects 174 W m^{-2} and absorbs 448 W m^{-2} of the available solar radiation which causes the surface to receive 604 W m^{-2}. For the no dust atmosphere, only 79 W m^{-2} of the 1226 W m^{-2} solar radiation available at the TOA is reflected while 238 W m^{-2} is absorbed which causes the surface to receive 909 W m^{-2}. Consequently, the dusty scenario absorbs 210 W m^{-2} more solar radiation in the atmosphere than in the no dust scenario which leads to the reduction of 305 W m^{-2} of solar radiation at the surface. After taking into account the minimal ocean reflectance, 174 W m^{-2} of solar radiation is leaving at the TOA in the dusty atmosphere as opposed to only 79 W m^{-2} in the no dust atmosphere. Thus, over this cloud-free water region from 10°N to 10.3°N, the TOA SWARE (black line in Figure 3b) is about −95 W m^{-2} due to the large AOD of about 1.7. By using the mean AOD of 1.7 along this section of the transect, a mean aerosol forcing efficiency (i.e., SWARE per unit AOD [*Christopher and Zhang*, 2004]) of approximately −56 W m^{-2} per AOD is calculated. Our TOA instantaneous SWARE of about −95 W m^{-2} is in good comparison to the −129 W m^{-2} measured for an AOD of about 1.5 during the Saharan Dust Experiment [*Haywood et al.*, 2003]. Note that the dust was slightly more reflecting in *Haywood et al.* [2003] with a ω_0 of 0.97 which will lead to a more negative TOA SWARE.

[24] The CALIPSO transect then encounters the low-level water clouds over the ocean from 10.3°N to 11.0°N causing the TOA SWARE due to dust to change from strongly negative to positive values. The low-level water clouds with an average COD of 9.3 cause an average TOA SWARE from 10.3°N to 11.0°N of 67 W m^{-2} (38 W m^{-2} per AOD) which means more outgoing energy is at the TOA in the cloud-only simulation compared to the cloud and dust simulation. The largest COD of 15 at 10.7°N leads to the most positive TOA SWARE value of 130 W m^{-2} (74 W m^{-2} per AOD). Therefore, the presence of the dust layer above the low-level water clouds reduces the outgoing solar radiation at the TOA since it absorbs a portion of the reflected radiation from the clouds along with reflecting a portion back toward the surface. The increased absorption of the dust layer above these low level clouds is clearly seen in Figure 3b as the SWARE in the atmosphere (blue line) increases to 267 W m^{-2} (about 152 W m^{-2} per AOD) at 10.7°N while the average value along this portion of the transect is 252 W m^{-2} (about 144 W m^{-2} per AOD). The increased background reflectance due to the low-level clouds causes the dust layer to receive more radiation from below which leads to the increased

absorption of radiation in the atmosphere. A similar response to low-level clouds beneath an absorbing aerosol layer was discussed in *Wilcox* [2010] as positive TOA SWAREs along with increased SW absorption were simulated for a case where clouds were beneath a smoke layer with a ω_0 of 0.89 at 550 nm. *Wilcox* [2010] also noted that the aerosol semidirect effect led to cloud thickening due to the increased solar absorption and heating of the smoke layer which increases the buoyancy and inhibits the entrainment of this above cloud air into the cloud layer. Therefore, the semidirect effect is most likely occurring in our case study as suggested by the increase in the absorbed solar radiation among the profiles with low-level clouds beneath dust, but the impact of the semidirect effect is probably much less here due to the considerably higher ω_0 for dust aerosols. Then, at the surface, a large increase to nearly −137 W m^{-2} (−78 W m^{-2} per AOD) is shown in Figure 3b (red line) at 10.7°N since the cloud alone significantly reduces the SW radiation received at the surface. The average SWARE at the surface from 10.3°N to 11.0°N in the cloudy profiles is −186 W m^{-2} (−106 W m^{-2} per AOD). A similar trend appears for the low-level clouds over land between 11.2°N and 11.4°N but the average SWARE values are considerably larger at the TOA and surface, which is mostly due to the increase in the average COD to 12.8. In fact, the most positive TOA SWARE value of 141 W m^{-2} (−84 W m^{-2} per AOD) occurs along this section of the transect which coincides with the highest COD of 19.

[25] After encountering the low-level clouds over land, the remainder of the transect (i.e., northward of 11.4°N) is less complex as only cloud-free dusty profiles are simulated. However, the varying albedo of the land along this transect significantly impacts the TOA and surface SWARE. From 11.4°N to 13.2°N, where the surface albedo is mostly between 15% and 25%, the mean SWARE at the TOA and surface is about −40 W m^{-2} (−24 W m^{-2} per AOD) and −253 W m^{-2} (−153 W m^{-2} per AOD), respectively. Then, at approximately 13.6°N, the TOA SWARE changes from negative to positive as the albedo increases to values greater than 30% which suggests there is a critical albedo of about 30% where the TOA SWARE goes from negative to positive. The critical albedo occurs when the albedo is insensitive to the AOD (e.g., TOA SWARE is 0 W m^{-2}). *Patadia et al.* [2009] found that the critical albedo can vary greatly over desert regions due to the different mineral dust types as absorbing dust types ($\omega_0 = 0.87$) can have a critical albedo just above 20% while a reflecting dust type ($\omega_0 = 0.97$) can have a critical albedo of 40%. Thus, the critical albedo of 30% for this dust layer with ω of approximately 0.95 agrees with the results of *Patadia et al.* [2009]. The mean TOA SWARE between 13.6 and 14.0°N is 10 W m^{-2} (6 W m^{-2} per AOD) with the maximum value of 18 W m^{-2} occurring at 14°N where the albedo is about 39%. Therefore, below the critical albedo of approximately 30%, the reflection of the dust layer leads to negative TOA SWARE. Above this critical albedo, the absorption of the dust leads to positive TOA SW radiative effect. The mean surface SWARE increases to −211 W m^{-2} (−132 W m^{-2} per AOD) between 13.6°N and 14.0°N as the highly reflecting surface negates some of the impact the dust layer has on reducing the absorbed SW radiative at the surface. Table 1 summarizes the radiative flux and SWARE results discussed in this section.

Table 1. Summary of the Radiative Flux and SWARE Results at the TOA, in the Atmosphere, and at the Surface Averaged Over the Cloud-Free Over Water (10°N–10.3°N), the Clouds Over Water (10.4°N–10.8°N), the Clouds Over Vegetated Land (11.2°N–11.4°N), the Cloud-Free Over Vegetated Land (11.4°N–13.2°N), and the Cloud-Free Over Bright Land (13.6°N–14.0°N) Sections Along the CALIPSO Transect[a]

Location	Type	SWARE (W m^{-2})				
		10.0°N–10.3°N	10.3°N–11.0°N	11.2°N–11.4°N	11.4°N–13.2°N	13.6°N–14.0°N
TOA	F_{cloud}	79	424	514	197	292
	$F_{dust+cloud}$	174	357	407	237	282
	SWARE	−95	67	107	−40	10
ATM	F_{cloud}	238	296	301	247	241
	$F_{dust+cloud}$	448	548	557	460	461
	SWARE	210	252	256	213	220
SFC	F_{cloud}	909	510	419	797	718
	$F_{dust+cloud}$	604	324	273	544	507
	SWARE	−305	−186	−146	−253	−211

[a]The radiative flux of the cloud only atmosphere is F_{cloud}, the radiative flux of the dust and cloud atmosphere is $F_{dust+cloud}$, and the difference between the two atmospheres gives the instantaneous SWARE.

4.2. SW and LW Heating Rates

[26] The elevated dust on 21 June 2007 leads to a SW heating of the atmosphere of greater than 6 K/d over a significant region of the dust layer from 4 to 7 km in height (Figure 5a). This shows that strong dust storms can have a very significant warming effect on the atmosphere due to their absorption properties. The largest SW heating rates occur when low-level clouds are present where the increased background reflectance of the clouds lead to more radiation received at the dust level and higher heating rates. The increased atmospheric SWARE where low clouds are present in Figure 3b means that more energy is absorbed in the atmosphere causing the higher SW heating rates within the dust layer above the clouds. Consequently, a significant area of SW heating rates larger than 10 K/d is simulated directly above the low clouds within the dust over both the water and land. For example, the low cloud with an optical depth of 8.6 at 11.2°N influences a SW heating rate of approximately 13.4 K/d. In the cloud-free dust profiles from 10°N to 10.4°N, a noticeable decrease in the SW heating rates is simulated due to the absence of low clouds beneath the dust. Also, note that the SW heating rates within the dust layer above cloud-free land (north of 11.4°N) show some regions of SW heating rates greater than 10 K/d even though the AOD is actually slightly decreasing along this portion of the transect. Again, this is explained by the higher surface albedo of the land that reflects more of the downwelling SW radiation at the surface upward into the dust layer. We also conducted a simulation where we held the AOD constant at 1.67 along the entire transect in order to see the impact the varying AOD has on the RTM calculations. Not surprisingly, the SW heating rates within the dust layer above the cloud-free land are slightly increased. Thus, the higher SW heating rates above the cloud-free land compared to the cloud-free ocean are more discernible in this constant AOD simulation (not shown).

[27] In the LW, there is a warming effect below the dust layer and a cooling effect near the top of the layer in Figure 5b as the dust absorbs the LW radiation and then reemits a considerable portion of the energy back toward the surface which leads to the increased LW heating rates below the dust layer. Due to the small dust particle size for this case, the LW heating rates are much smaller in the

cloud-free areas with maximum heating of about 0.8 K/d and minimum cooling of about −1.5 K/d. When comparing the LW heating rates at 10.5°N to that at 11.2°N, the atmosphere with the COD of 12.4 has a minimum value of −1.0 K/d while the atmosphere with the COD of 8.6 has a minimum value of −1.3 K/d. The stronger LW cooling occurring in the atmosphere with the lower COD at 11.2°N is mostly due to the cloud absorbing less LW radiation from the surface than the
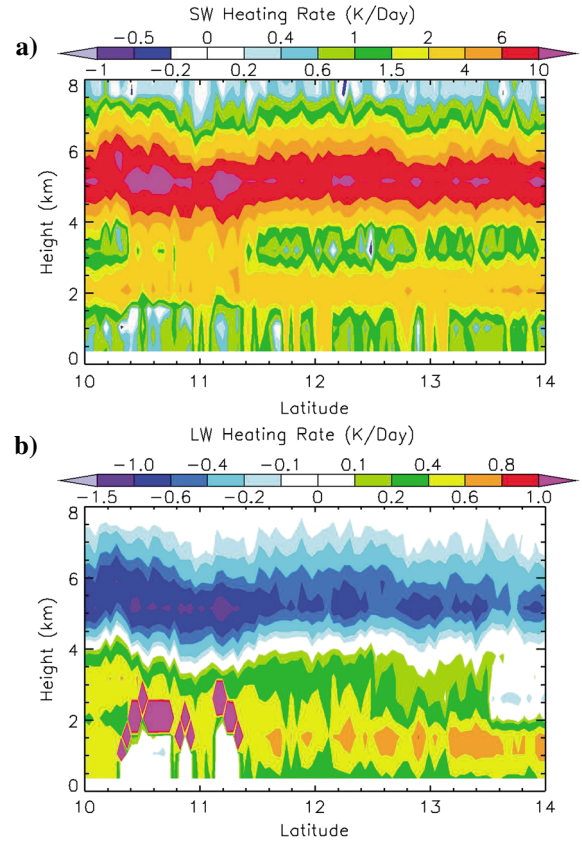

Figure 5. (a) SW radiative heating rates simulated by the delta-four stream RTM along the transect from 10°N to 14°N on 21 June 2007. (b) Similar to Figure 5a but for LW radiative heating rates.

Table 2. RTM Results for the SWARE Averaged Over the Various Sections of the CALIPSO Transect as Done in Table 1[a]

Location	AOD	SWARE (W m^{-2})				
		10.0°N–10.3°N	10.3°N–11.0°N	11.2°N–11.4°N	11.4°N–13.2°N	13.6°N–14.0°N
TOA	1.25	−74	60	91	−27	14
	2.09	−117	76	123	−50	6
ATM	1.25	163	208	208	170	171
	2.09	250	293	296	261	265
SFC	1.25	−238	−148	−117	−196	−157
	2.09	−368	−217	−173	−309	−259

[a]However, instead of using the AOD of 1.67 calculated from the BAE-146 extinction profile, the lower (1.25) and upper bounds (2.09) of the AOD uncertainty range are used in the model simulation.

optically thicker cloud at 10.5°N. Therefore, more LW radiation is absorbed beneath the dust at 11.2°N which then leads to stronger cooling within the dust layer. Note that the same GFS atmospheric profiles were used to simulate the RTM at these two locations. Even though we are subtracting F_{cloud} from $F_{dust+cloud}$ in order to remove the impacts of cloud, the largest LW heating rates still appear within the cloud layers in Figure 5b due to the dust layer absorbing and reemitting LW radiation back toward the cloud layers. Thus, the cloud layers are receiving more energy in the dusty atmosphere than in the dust-free atmosphere which influences the LW heating rates of up to 5 K/d near the cloud tops. Conversely, in the SW, a few of the cloud layers in the dusty atmosphere are associated with a weak SW cooling since less downwelling radiation is received at the cloud top when dust is above as opposed to clear sky above.

[28] *Quijano et al*. [2000] conducted a cloud-free RTM simulation for suspended dust layer from 1 to 4 km in height for a high sun angle (SZA ~ 35°) over a desert-like surface with an albedo of 30%, and they found SW heating rates of about 6 K/d within the dust layer. In our study, considerably higher SW heating rates of 10.5 K/d are simulated within the cloud-free atmosphere at 13.4°N where the surface albedo is about 30% and SZA about 25°. The higher SW heating rate in our study is due mostly to the dust layer having a much higher AOD at 0.5 μm of nearly 1.7 compared to the AOD of 0.5 used in *Quijano et al*. [2000]. In fact, the difference in the SW heating rates could have been even larger, but *Quijano et al*. [2000] used unrealistically low ω_0 values of less than 0.9 for the visible wavelengths which causes the dust layer to absorb too much solar radiation leading to unrealistic heating rates. An additional RTM simulation was conducted in *Quijano et al*. [2000] over an ocean surface with an albedo of 5% where they inserted a low cloud (COD = 10) beneath a dust layer (AOD = 1). Their results showed maximum NET (SW + LW) heating rates of nearly 8 K/d within the dust layer. When the dust layer was removed (e.g., AOD = 0), the NET heating rates decreased to only about 0.5 K/d within the atmosphere. Consequently, the presence of the dust layer above the low cloud caused an additional warming of 7.5 K/d within the atmosphere. Similar warming effects are observed within dust layers above clouds in our study. For instance, if we look again at 10.5°N, the maximum NET heating rate within the dust layer (AOD = 1.7) is about 10.5 K/d since the SW and LW heating rates were 11.5 and −1.0 K/d, respectively. Even though *Quijano et al*. [2000] use a significantly lower ω_0, the combination of the optically thicker cloud (COD = 12.4) and dust layer in our study influences the larger NET heating rates.

Furthermore, the RTM simulations in *Huang et al*. [2009] also showed the significant radiative impacts of dust aerosols in the atmosphere as a dust storm (AOD = 0.8) over a cloud-free desert surface with an albedo of 35% influenced SW and LW heating rates of 7 and −1.5 K/d, respectively. Note that these are daily averaged heating rates that are not directly comparable to our instantaneous heating rates. Also, *Huang et al*. [2009] used an unrealistically low ω_0 of 0.89 at 0.67 μm in their simulations. Nonetheless, for a very similar surface albedo at 13.8°N, our study found SW and LW heating rates of 10 and −0.7 K/d within the dust layer (AOD = 1.56).

4.3. Uncertainties and Sensitivity Analysis

[29] In our study, we reduce the uncertainties by using as many available observations as possible for critical RTM inputs such as ω_0, g, and effective radius retrieved from the Dakar AERONET station and the AOD measured by the BAE-146 aircraft. The uncertainties for all these aerosol properties are discussed in section 2. However, the Dakar station at 14.4°N and 16.9°W is just north of the dust layer analyzed in this study. Thus, the measurements at the Dakar station may not be completely representative of the dust layer especially its southern extent at 10°N. We also used a constant ω_0, g, and effective radius for the entire dust layer when in reality there would be variability in these parameters. The significant uncertainties with using CALIPSO data are reduced by deriving our own extinction profiles from the accurate level 1B data. The extinction profiles were derived by comparing an accurate BAE-146 aircraft extinction profile to the nearest CALIPSO level 1B profile and finding the lidar ratio values that most accurately fit the derived CALIPSO extinction profile to the BAE-146 profile. However, this fitting technique was performed at the location of the BAE-146 profile (16.6°N, 16°W) which was north of the dust layer analyzed in this study. The CloudSat retrievals used in this study can also contribute to the uncertainty but we use the CloudSat cloud mask to only retain clouds detected with very high confidence.

[30] Since the BAE-146 extinction profile has a major impact on the fitted extinctions that are input into the model, we assess the impact of the BAE-146 extinction errors estimated at ±25% on the radiative fluxes simulated by the model. The ±25% error in extinction leads to an uncertainty range of AOD in this study of 1.67 ± 0.42. Table 2 shows the RTM results for the SWARE averaged over the various sections of the CALIPSO transect as done in Table 1. However, instead of using the AOD of 1.67 calculated from the BAE-146 extinction profile, the lower (1.25) and upper bounds (2.09) of the AOD uncertainty range are used in the

Table 3. Similar to Table 2 Except That RTM Results for the 2.0 μm and 4.0 μm Mineral Dust Sizes Are Presented

Location	Size (μm)	SWARE (W m^{-2})				
		10.0°N–10.3°N	10.3°N–11.0°N	11.2°N–11.4°N	11.4°N–13.2°N	13.6°N–14.0°N
TOA	2.0	−67	113	153	−8	44
	4.0	−43	149	192	15	71
ATM	2.0	264	315	318	273	279
	4.0	312	370	374	321	331
SFC	2.0	−331	−203	−164	−281	−235
	4.0	−355	−221	−181	−306	−260

model simulation. When comparing the SWARE calculations in Table 1 to Table 2, the values show considerable differences in magnitude especially in the atmosphere and at the surface which is expected with an AOD range of 1.25–2.09. Nevertheless, it is important to note that the sign of the SWARE values at the TOA does not change. Therefore, the dust still causes an overall warming at the TOA between 10.3°N–11.0°N and 11.2°N–11.4°N, and an overall cooling at the TOA occurs between 10°N–10.3°N, 11.4°N–13.2°N, and 13.6°N–14.0°N.

[31] Finally, we conduct a sensitivity analysis on the impact of the differing prescribed optical property values for several mineral dust sizes on the radiative fluxes and heating rates simulated by the RTM. As already discussed, we chose the 1.0 μm dust size since the nearby Dakar AERONET station retrieved a dust effective radius of 1.1 μm for this dust storm. We reduced the dependency on the prescribed optical properties in the model by inputting extinction coefficient profiles derived from CALIPSO data and inputting ω and g retrieved by the Dakar station into bands 1 (0.2–0.7 μm) and 2 (0.7–1.3 μm) of the RTM. However, we still rely on the prescribed optical property values for the remaining 4 SW bands and 12 LW bands. Therefore, we conduct two additional RTM simulations where we use the prescribed optical properties (i.e., extinction coefficients, ω, and g) for the 2.0 and 4.0 μm mineral dust sizes to understand the sensitivity of the model to the chosen dust size. The general pattern of the RTM results for the 1.0 μm dust size in Figures 4 and 5 is still apparent for the 2.0 and 4.0 μm dust sizes such as the large SWARE increases that occur at the TOA, within the atmosphere, and at the surface in the low cloud profiles and the increase of the TOA and surface SWARE as the albedo increases. Also, the maximum SW heating rates still appear in the dust layer above the low cloud profiles and the maximum LW heating rates still appear within the low clouds with the largest LW cooling rates near the top of the dust layer. Nevertheless, quantitatively, the RTM results are much different for the 2.0 and 4.0 μm dust sizes as shown in Table 3 which is similar to Table 2 except that RTM results for the 2.0 and 4.0 μm mineral dust sizes are presented.

[32] When comparing the SWARE in Tables 1 and 3, the values at TOA and atmosphere significantly increase while the values at the surface significantly decrease when inputting these large dust sizes into the model. For instance, the TOA SWARE increases from 67 W m^{-2} for the 1.0 μm size to 149 W m^{-2} for the 4.0 μm size between 10.3°N and 11.0°N and similar increases are shown for the other sections along the CALIPSO transect. In fact, the TOA SWARE increases from a negative value of −40 W m^{-2} for the 1.0 μm size to a positive value of 15 W m^{-2} for the 4.0 μm

size between 11.4°N and 13.2°N. Thus, the 4.0 μm dust has an overall warming effect at the TOA between 11.4°N and 13.2°N as opposed to the cooling effect simulated for the 1.0 and 2.0 μm dust. As expected, since the SWAREs in the atmosphere significantly increase with dust particle size, the SW heating rates also increase significantly as the mean values within the main region of the dust storm from 4 to 8 km in height are about 4.6 for 1.0 μm dust, 5.7 for 2.0 μm dust, and 6.6 K/d for 4.0 μm dust. The decreasing ω_0 with increasing dust size prescribed in RTM bands 3–6 is the major cause of these differences as the 2.0 μm dust size has primarily lower values compared to 1.0 μm with a maximum difference in band 3 (1.3–1.9 μm) where the 1.0 and 2.0 μm sizes have ω_0 values of 0.96 and 0.92, respectively. The 4.0 μm size has significantly lower ω_0 than 1.0 μm with differences of 9 to 10% in bands 3–5 with the largest difference in band 3 where 4.0 μm has a ω_0 of 0.86. Thus, the RTM is very sensitive to the specific ω_0 value used in the SW bands and the model results can vary greatly based on the mineral dust particle size as the larger dust particles are much more absorbing than the smaller particles.

[33] In the LW, we rely strictly on the prescribed optical properties in the RTM since we have no measurements of these optical properties in the LW for this case study. Using the 2.0 μm instead of the 1.0 μm dust particle causes the mean TOA LW flux along the transect from 10°N to 14°N to decrease from about 272 to 255 W m^{-2}. Further increasing the dust particle size input to 4.0 μm causes the mean TOA LW flux to decrease to about 246 W m^{-2}. Consequently, the LW heating and cooling rates are significantly different for the 2.0 and 4.0 μm dust sizes as the mean LW heating rate from 1 to 5 km in height along the transect from 10°N to 14°N is 1.2 K/d for the 4.0 μm size and only 0.4 K/d for the 1.0 μm size. Thus, much more heating takes place beneath and within the dust storm when the dust particle size is larger. Also, the LW cooling that occurs near the top of the dust storm in Figure 5b for the 1.0 μm size increases for the 4.0 μm size as the mean LW cooling rates from 10°N to 14°N for the 1.0 and 4.0 μm sizes are 0.3 and 0.6 K/d, respectively. We then conduct a sensitivity experiment where we replace the 1.0 μm dust optical properties with the 4.0 μm dust optical properties which showed that the prescribed extinction coefficients are the major cause of these differences in the LW fluxes and ultimately the LW heating rates. The prescribed extinction coefficients in the LW bands are vastly different between the 1.0, 2.0, and 4.0 μm dust sizes as the 2.0 μm size has extinction coefficients ranging from 0.21 to 1.20 km^{-1} while the 1.0 μm size has extinction coefficients ranging from 0.05 to 0.53 km^{-1}. The 4.0 μm size has even larger extinction coefficients that range from 0.54 to 1.4 km^{-1} in the 12 LW bands. Thus, these much larger extinction coefficients for the
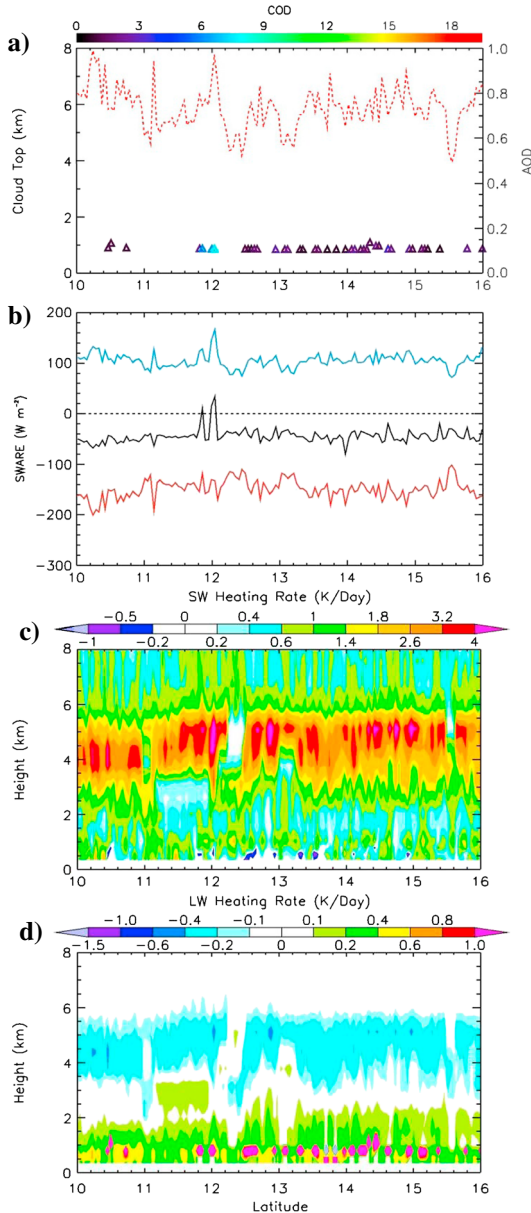
Figure 6. Same as Figures (a, b) 3 and (c, d) 5 but for RTM results for 18 June 2007 case.

larger dust particles lead to significantly more heating within the dust layer and more cooling near the top of the dust layer.

4.4. Additional Case Studies

[34] We simulate two additional case studies involving dust above low-level clouds using the same technique and data sources as those applied to the 21 June 2007 case except that we do not have BAE-146 aircraft data. We used the extinction profiles and AOD from the BAE-146 aircraft for the 21 June case due to the complete attenuation of the CALIOP signal through the intense dust storm. The CALIOP signal does not experience complete attenuation through the dust layers of the additional case studies since the AOD is much lower. Therefore, the BAE-146 extinction profiles and AOD are not necessary for these additional cases since we can use the extinction and AOD derived from

CALIPSO. Furthermore, ω_0 and g are computed from the AERONET station at Cape Verde since it is the closest station, but Cape Verde is still about 1000 km to the west. However, HYSPLIT backward trajectories showed that the dust was over Cape Verde the day prior to the case studies. Therefore, the ω_0 and g input into the RTM for these additional cases were retrieved from the Cape Verde station approximately 24 h prior to the time of the cases. There are negligible differences in the SZA between these cases as they vary between 22°N and 26°N.

[35] On 18 June 2007 at approximately 1540 UTC, CALIPSO passed over a dust layer between 2 and 6 km in height over the western Atlantic Ocean. We analyze the portion of the transect from 10°N to 16°N where low-level clouds resided beneath the dust. For RTM bands 1 and 2, the ω_0 values are 0.93 and 0.98 while the g values are 0.77 and 0.75. The AODs derived from the CALIPSO measurements along the transect are shown in Figure 6a where the values range mostly between 0.6 and 1.0. The CODs from CloudSat are much lower than that for the 21 June case as they are generally between 0 and 4 except for the CODs from 6 to 8 near 12°N. Note that we do not show the surface albedo for these additional case studies since they are both over water with a consistent broadband albedo of 3% throughout the transect. For this 18 June case, the TOA SWARE ranges between -80 and -20 W m^{-2} except at the location of the optically thicker clouds near 12°N where the values are positive (Figure 6b). The SWARE in the atmosphere significantly increases when optically thicker clouds (COD > 6) are present as they reflect greater amounts of solar radiation upward into the dust layer than the background water surface or the optically thinner clouds (COD < 4). For the COD of 7.2, the SWARE at the TOA is 34 W m^{-2}, in the atmosphere is 166 W m^{-2}, and at the surface is -132 W m^{-2}. Conversely, for the cloud-free profile at 10.3°N with a nearly identical AOD of 0.96, the SWARE at the TOA is -64 W m^{-2}, in the atmosphere is 129 W m^{-2}, and at the surface is -194 W m^{-2}. Thus, as observed in the 21 June case, clouds beneath dust can cause a warming at the TOA, more absorption of solar radiation within the dust, and a reduction in the surface cooling compared to a cloud-free dust atmosphere.

[36] The SW heating rates for 18 June are much lower than for 21 June but we still see heating rates from about 1.5 to 6.5 K/d for most of the dust layer (Figure 6c). Not surprisingly, the largest SW heating rate of 6.5 K/d occurs within the dust directly above the cloud with the largest COD of 7.2. The SW cooling rates within the clouds are more apparent for this case compared to 21 June since less dust is present in the low-level atmosphere to mask the cooling effect of the clouds. For example, the COD of 7.2 influences a SW cooling rate of about -0.4 K/d in the lowest 1 km of the atmosphere. The LW cooling rates are also lower for this case since the dust is optically thinner than on 21 June with values generally ranging from -0.7 to -0.2 K/d (Figure 6d). Once again, LW warming rates greater than 1 K/d are simulated within the low-level clouds as the dust layer above absorbs and reemits a portion of the LW radiation back toward the clouds. The largest LW warming rate of 5 K/d occurs within the cloud having the largest COD of 7.2.

[37] The CALIOP lidar measures another dust layer suspended between 2 and 5 km over the eastern Atlantic
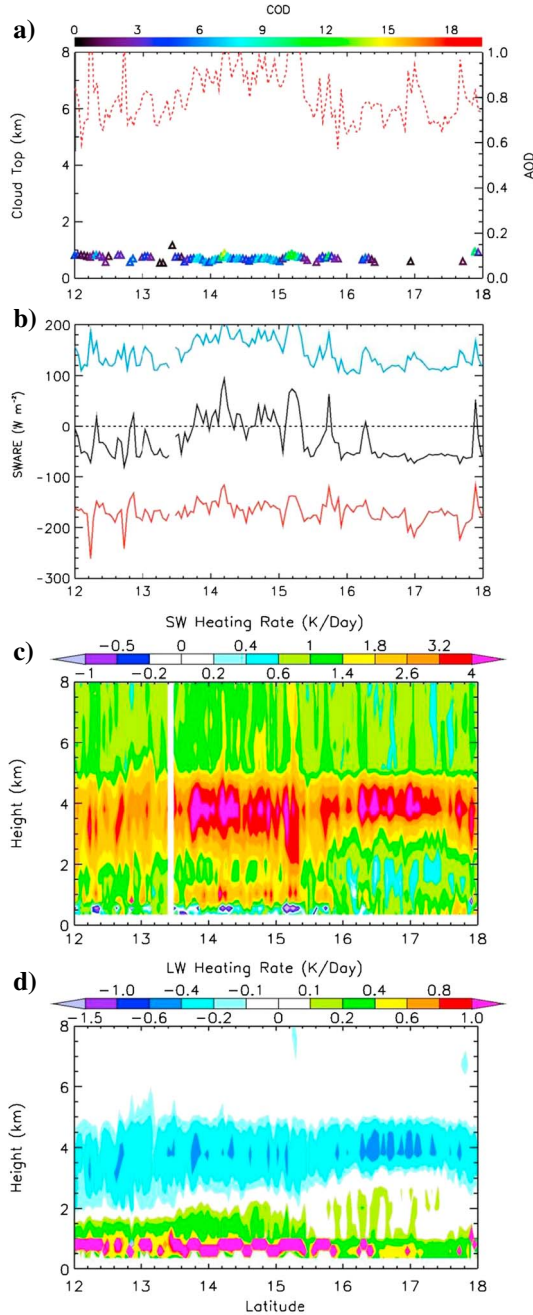
11

Figure 7. Same as Figure 6 but for RTM results for 31 May 2007 case.

Ocean on 31 May 2007 at approximately 1600 UTC. The ω_0 retrieved by the Cape Verde station suggests the dust layer is slightly less absorbing than the dust on 18 June while the g values show negligible differences. For this case, ω_0 of 0.94 and 0.98 are input into the RTM bands 1 and 2. More low-level clouds with higher COD are detected by CloudSat for this case than on 18 June, especially from 13.5°N to 15.5°N where the average COD is about 6 with a maximum value of 12.7 (Figure 7a). Consequently, the mean TOA SWARE along this cloudy portion of the transect is about 14 W m^{-2} with the maximum value of 94 W m^{-2} occurring in the profile at 14.2°N where the COD of 12.7 (Figure 7b). The COD of 12.7 also influences an increase in the SWARE in

the atmosphere to 210 W m^{-2} and at the surface to -116 W m^{-2}. However, this profile is also associated with one of the largest AODs of 1.2 so we compare it to a cloud-free profile with a similar AOD at 12.7°N. At 12.7°N, the SWARE at the TOA, in the atmosphere, and at the surface is -81, 160, and -241 W m^{-2}, respectively. The substantial differences between the SWARE values further confirms the major impact that low clouds can have on the radiative energy budget of a dust storm.

[38] When examining the heating rates, a larger area of the dust layer is associated with SW heating rates greater than 3.2 K/d for this case than for 18 June, which is very apparent in the portion of the transect from 13.5°N to 15.5°N where the average COD is about 6 (Figure 7c). However, the maximum SW heating rates are actually slightly lower within this dust layer due to the AOD being spread over a larger vertical depth in the atmosphere. For instance, in the profile with the COD of 12.7 at 14.2°N, the maximum SW heating rate is 5.3 K/d at about 4 km in height which is lower than the maximum rate of 6.5 K/d for the profile with the COD of 7.2 on 18 June. Nevertheless, SW heating rates greater than 1.8 K/d are simulated over a vertical depth of 4 km for this case as opposed to only 2 km for 18 June. As expected, the optically thickest clouds at 14.2°N and 15.2°N are associated with the strongest SW cooling rates of -1.3 and -2.1 K/d, respectively. Similar LW heating and cooling rates are shown for this case compared to June 18 as warming rates are generally from 0.2 to 0.6 K/d within the cloud-free areas beneath the dust layer and -0.2 to -0.6 K/d within the dust layer (Figure 7d). Though, noteworthy differences appear within the cloud layers beneath the dust layer as the optically thicker clouds are influencing higher LW heating rates of up to 6 K/d.

[39] Finally, we conduct idealistic RTM simulations for the 18 June and 31 May case studies where the AOD is held constant at 0.8 for both simulations. We use an AOD of 0.8 as it is about the average value for the two cases. We also used the same ω_0 and g values for these idealistic simulations which were identical to that used for the 31 May case. The average SWAREs at the TOA, in the atmosphere, and at the surface for a range of CODs occurring in these two cases are presented in Table 4. In the cloud-free profiles, the dust influences a cooling of -54 W m^{-2} at the TOA over the eastern Atlantic Ocean. However, when the profiles contain low-level clouds with COD from 8 to 13, the dust influences a warming of 53 W m^{-2} at the TOA. For these two cases, we found that the TOA SWARE is very near 0 when the COD is between 4 and 5. The SWARE in the atmosphere gradually increased with increasing COD due to the dust layer absorb-

Table 4. The Average SWARE at the TOA, in the Atmosphere (ATM), and at the Surface (SFC) for Different COD Bins Occurring in the 31 May and 18 June Cases

COD	SWARE (W m^{-2})		
	TOA	ATM	SFC
0	-54	110	-164
0–4	-38	122	-159
4–5	2	136	-134
5–8	20	140	-120
8–13	53	148	-95

ing more solar radiation from the higher reflectance of the low-level clouds. At the surface, dust influences a strong cooling of -164 W m^{-2} in cloud-free profiles, but the cooling effect decreases to -95 W m^{-2} in profiles with a COD from 8 to 13 since optically thick clouds reflect significant amounts of energy away from the surface.

5. Summary and Conclusions

[40] In this study, we use the CALIPSO and CloudSat observations as input into a delta-four stream RTM in order to simulate a case study involving an intense dust storm with low-level clouds. In addition, we use AERONET station and aircraft flight data to simulate the RTM with the most appropriate and accurate input information. RTM simulations using similar inputs are also conducted for two additional case studies involving low-level cloud beneath dust on 31 May and 18 June 2007. This study is unique because we simulate a RTM on a case study having clouds beneath dust and input the complex vertical atmospheric information by combining the strengths of the CALIPSO and CloudSat satellites. Our results indicate the following:

[41] 1. The presence of low-level clouds beneath a dust storm can cause important modifications in the radiative energy budget. For the 21 June 2007 dust storm, the instantaneous TOA SWARE over the ocean changed from an average of -95 (-58 W m^{-2} per AOD) in the cloud-free dusty conditions to 67 W m^{-2} (38 W m^{-2} per AOD) in the cloud beneath dust conditions where the average COD was 9.3. This shows the potential for mineral dust aerosol to have either a cooling or warming effect on regional or global climate depending on whether low-level clouds reside below dust layers. In the atmosphere, the average SWARE was 252 W m^{-2} (144 W m^{-2} per AOD) when low-level clouds were beneath dust as opposed to 210 W m^{-2} (124 W m^{-2} per AOD) in the cloud-free conditions. Thus, low-level clouds can reflect more solar radiation upward into the dust layer compared to the background ocean or land surface which influences a larger absorption of energy within the dust. Dust also significantly reduced the solar radiation at the surface as the SWARE in cloud-free conditions was about -305 W m^{-2} (-180 W m^{-2} per AOD). However, the reduction in the solar radiation at the surface due to dust was only about -186 W m^{-2} (-106 W m^{-2} per AOD) when low-level clouds were present since clouds alone can reflect substantial amounts of energy away from the surface.

[42] 2. The surface albedo has an important impact on the SWARE of dust. For the 21 June 2007 case, we found a critical surface albedo of approximately 30%, i.e., the TOA SWARE went from negative to positive in the cloud-free dusty atmosphere as surface albedos rose above 30%. Over the cloud-free ocean, the SWARE was about -95 W m^{-2}, while over the adjacent land with a broadband albedo of about 18%, the SWARE was -38 W m^{-2}.

[43] 3. Dust storms can cause a significant warming in the atmosphere. SW heating rates greater than 10 K/d were found within the dust and the largest heating rates typically occurred where low-level clouds resided beneath the dust. LW cooling effects within the dust layer can compensate for some of SW heating effects but for these dust cases consisting of smaller particles (~1 μm) the SW heating effect dominated.

[44] 4. The LW warming rates within low-level clouds in dusty conditions can significantly increase compared to that in dust-free conditions due to the dust emitting LW radiation toward the clouds. We found warming rates as large as 6 K/d within the clouds which generally increased with increasing COD.

[45] The major conclusion from this paper is that low-level clouds beneath dust aerosols can cause significant changes in both the SWARE and SW and LW heating rates. Therefore, it is critical that we identify and study scenarios where clouds exist among dust in order to gain knowledge of their possible impacts on regional and global radiation budgets. While such intensive case studies cannot provide global estimates of such effects, they highlight and quantify the relative importance of various processes and interactions that need to be captured in global and regional models to accurately assess of aerosol radiative forcings and climate impacts.

References

Ackerman, S. A. (1997), Remote sensing aerosols using satellite infrared observations, *J. Geophys. Res.*, *102*(D14), 17,069–17,079, doi:10.1029/96JD03066.

Chand, D., T. L. Anderson, R. Wood, R. J. Charlson, Y. Hu, Z. Liu, and M. Vaughan (2008), Quantifying above-cloud aerosol using spaceborne lidar for improved understanding of cloudy-sky direct climate forcing, *J. Geophys. Res.*, *113*, D13206, doi:10.1029/2007JD009433.

Christopher, S. A., and J. Zhang (2002), Shortwave aerosol radiative forcing from MODIS and CERES observations over the oceans, *Geophys. Res. Lett.*, *29*(18), 1859, doi:10.1029/2002GL014803.

Christopher, S. A., and J. Zhang (2004), Cloud-free shortwave aerosol radiative effect over oceans: Strategies for identifying anthropogenic forcing from Terra satellite measurements, *Geophys. Res. Lett.*, *31*, L18101, doi:10.1029/2004GL020510.

Devasthale, A., and M. A. Thomas (2011), A global survey of aerosol-liquid water cloud overlap based on four years of CALIPSO-CALIOP data, *Atmos. Chem. Phys.*, *11*, 1143–1154, doi:10.5194/acp-11-1143-2011.

Dubovik, O., A. Smirnov, B. N. Holben, M. D. King, Y. J. Kaufman, T. F. Eck, and I. Slutsker (2000), Accuracy assessments of aerosol optical properties retrieved from Aerosol Robotic Network (AERONET) Sun and sky radiance measurements, *J. Geophys. Res.*, *105*(D8), 9791–9806, doi:10.1029/2000JD900040.

Formenti, P., M. O. Andreae, and J. Lelieveld (2000), Measurements of aerosol optical depth above 3570 m asl in the North Atlantic free troposphere: Results from ACE-2, *Tellus, Ser. B*, *52*, 678–693.

Forster, P., et al. (2007), Changes in atmospheric constituents and in radiative forcing, in *Climate Change 2007: The Physical Science Basis. Contribution of Working Group I to the Fourth Assessment Report of the Intergovernmental Panel on Climate Change*, edited by S. Solomon et al., chap. 2, pp. 131–234, Cambridge Univ. Press, Cambridge, U K.

Fu, Q., and K.-N. Liou (1992), On the correlated k-distribution method for radiative transfer in nonhomogenous atmospheres, *J. Atmos. Sci.*, *49*, 2139–2156.

Fu, Q., and K.-N. Liou (1993), Parameterization of the radiative properties of cirrus clouds, *J. Atmos. Sci.*, *50*, 2008–2025.

Hair, J. W., C. A. Hostetler, A. L. Cook, D. B. Harper, R. A. Ferrare, T. L. Mack, W. Welch, L. R. Isquierdo, and F. E. Hovis (2008), Airborne high spectral resolution lidar for profiling aerosol optical properties, *Appl. Opt.*, *47*, 6734–6752, doi:10.1364/AO.47.006734.

Haywood, J. M., and O. Boucher (2000), Estimates of the direct and indirect radiative forcing due to tropospheric aerosols: A review, *Rev. Geophys.*, *38*(4), 513–543, doi:10.1029/1999RG000078.

Haywood, J., P. Francis, S. Osborne, M. Glew, N. Loeb, E. Highwood, D. Tanré, G. Myhre, P. Formenti, and E. Hirst (2003), Radiative properties and direct radiative effect of Saharan dust measured by the C-130 aircraft during SHADE: 1. Solar spectrum, *J. Geophys. Res.*, *108*(D18), 8577, doi:10.1029/2002JD002687.

Haywood, J. M., et al. (2011), Motivation, rationale and key results from the GERBILS Saharan dust measurement campaign, *Q. J. Roy. Meteorol. Soc.*, *137*, 1106–1116, doi:10.1002/qj.797.

Holben, B. N., et al. (1998), AERONET - A federated instrument network and data archive for aerosol characterization, *Remote Sens. Environ.*, *66*, 1–16.

Huang, J., P. Minnis, B. Chen, Z. Huang, Z. Liu, Q. Zhao, Y. Yi, and J. K. Ayers (2008), Long-range transport and vertical structure of Asian dust from CALIPSO and surface measurements during PACDEX, *J. Geophys. Res.*, *113*, D23212, doi:10.1029/2008JD010620.

Huang, J., Q. Fu, J. Su, Q. Tang, P. Minnis, Y. Hu, Y. Yi, and Q. Zhao (2009), Taklimakan dust aerosol radiative heating derived from CALIPSO observations using the Fu-Liou radiation model with CERES constraints, *Atmos. Chem. Phys.*, *9*, 4011–4021, doi:10.5194/acp-9-4011-2009.

Johnson, B. T., and S. R. Osborne (2011), Physical and optical properties of mineral dust aerosol measured by aircraft during the GERBILS campaign, *Q. J. Roy. Meteorol. Soc.*, *137*, 1,117–1,130, doi:10.1002/qj.777.

Liu, D., Z. Wang, Z. Liu, D. Winker, and C. Trepte (2008), A height resolved global view of dust aerosols from the first year CALIPSO lidar measurements, *J. Geophys. Res.*, *113*, D16214, doi:10.1029/2007JD009776.

Liu, Z., D. Winker, A. Omar, M. Vaughan, C. Trepte, Y. Hu, K. Powell, W. Sun, and B. Lin (2011), Effective lidar ratios of dense dust layers over North Africa derived from the CALIOP measurements, *J. Quant. Spectrosc. Radiat. Transfer*, *112*, 204–213, doi:10.1016/j.jqsrt.2010.05.006.

Mace, G. G., Q. Zhang, M. Vaughan, R. Marchand, G. Stephens, C. Trepte, and D. Winker (2009), A description of hydrometeor layer occurrence statistics derived from the first year of merged CloudSat and CALIPSO data, *J. Geophys. Res.*, *114*, D00A26, doi:10.1029/2007JD009755.

Naeger, A. R., S. A. Christopher, R. Ferrare, and Z. Liu (2013), A new technique using infrared satellite measurements to improve the accuracy of the CALIPSO cloud-aerosol discrimination method, *IEEE Trans. Geosci. Remote Sens.*, *51*(1), 642–653, doi:10.1109/TGRS.2012.2201161.

Osborne, S. R., B. T. Johnson, J. M. Haywood, A. J. Baran, M. J. Harrison, and C. L. McConnell (2008), Physical and optical properties of mineral dust aerosol during the Dust and Biomass-Burning Experiment, *J. Geophys. Res.*, *113*, D00C03, doi:10.1029/2007JD009551.

Patadia, F., E.-S. Yang, and S. A. Christopher (2009), Does dust change the clear sky top of atmosphere shortwave flux over high surface reflectance regions?, *Geophys. Res. Lett.*, *36*, L15825, doi:10.1029/2009GL039092.

Powell, K. A., et al. (2009), CALIPSO lidar calibration algorithms. Part I: Nighttime 532-nm parallel channel and 532-nm perpendicular channel, *J. Atmos. Oceanic Tech.*, *26*, 2015–2033, doi:10.1175/2009JTECHA1242.1.

Qu, J. J., X. Hao, M. Kafatos, and L. Wang (2006), Asian dust storm monitoring combining Terra and Aqua MODIS SRB measurements, *IEEE Geosci. Remote Sens. Lett.*, *3*(4), 484–486, doi:10.1109/LGRS.2006.877752.

Quijano, A. L., I. N. Sokolik, and O. B. Toon (2000), Radiative heating rates and direct radiative forcing by mineral dust in cloudy atmospheric conditions, *J. Geophys. Res.*, *105*(D10), 12,207–12,219, doi:10.1029/2000JD900047.

Rogers, R. R., et al. (2011), Assessment of the CALIPSO Lidar 532 nm attenuated backscatter calibration using the NASA LaRC airborne High Spectral Resolution Lidar, *Atmos. Chem. Phys.*, *11*, 1295–1311, doi:10.5194/acp-11-1295-2011.

Rose, F. G., and T. P. Charlock (2002), New Fu-Liou code tested with ARM Raman lidar and CERES in pre-CALIPSO exercise. Extended abstract for 11th Conference on Atmospheric Radiation (AMS), 3–7 June 2002 in Ogden, Utah.

Schaaf, C. B., et al. (2002), First operational BRDF, albedo nadir reflectance products from MODIS, *Remote Sens. Environ.*, *83*, 135–148.

Schuster, G. L., M. Vaughan, D. MacDonnell, W. Su, D. Winker, O. Dubovik, T. Lapyonok, and C. Trepte (2012), Comparison of CALIPSO aerosol optical depth retrievals to AERONET measurements, and a climatology for the lidar ratio of dust, *Atmos. Chem. Phys. Discuss.*, *12*, 11,641–11,697, doi:10.5194/acpd-12-11641-2012.

Sokolik, I. N. (2002), The spectral radiative signature of wind-blown mineral dust: Implications for remote sensing in the thermal IR region, *Geophys. Res. Lett.*, *29*(24), 2154, doi:10.1029/2002GL015910.

Stephens, G. L., et al. (2002), The CloudSat mission and the A-Train, *Bull. Am. Meteorol. Soc.*, *83*, 1,771–1,790, doi:10.1175/BAMS-83-12-1771.

Stephens, G. L., et al. (2008), CloudSat mission: Performance and early science after the first year of operation, *J. Geophys. Res.*, *113*, D00A18, doi:10.1029/2008JD009982.

Tegen, I., and A. A. Lacis (1996), Modeling of particle size distribution and its influence on the radiative properties of mineral dust aerosol, *J. Geophys. Res.*, *101*, 19,237–19,244.

Tesche, M., A. Ansmann, D. Müller, D. Althausen, R. Engelmann, M. Hu, and Y. Zhang (2007), Particle backscatter, extinction, and lidar ratio profiling with Raman lidar in south and north China, *Appl. Opt.*, *46*(25), 6302–6308.

Wilcox, E. M. (2010), Stratocumulus cloud thickening beneath layers of absorbing smoke aerosol, *Atmos. Chem. Phys.*, *10*, 11,769–11,777, doi:10.5194/acp-10-11769-2010.

Winker, D. M., J. R. Pelon, and M. P. McCormick (2003), The CALIPSO mission: Spaceborne lidar for observation of aerosols and clouds, *Proc. SPIE-Int. Soc. Opt. Eng.*, *4893*, 1–11.

Winker, D. M., M. A. Vaughan, A. Omar, Y. Hu, K. A. Powell, Z. Liu, W. H. Hunt, and S. A. Young (2009), Overview of the CALIPSO mission and CALIOP data processing algorithms, *J. Atmos. Oceanic Technol.*, *26*, 2310–2323, doi:10.1175/2009JTECHA1281.1.

Yang, E.-S., P. Gupta, and S. A. Christopher (2009), Net radiative effect of dust aerosols from satellite measurements over Sahara, *Geophys. Res. Lett.*, *36*, L18812, doi:10.1029/2009GL039801.

Zhang, J. L., and S. A. Christopher (2003), Longwave radiative forcing of Saharan dust aerosols estimated from MODIS, MISR, CERES observations on Terra, *Geophys. Res. Lett.*, *30*(23), 2188, doi:10.1029/2003GL018479.

Zhang, Y., W. B. Rossow, A. A. Lacis, V. Oinas, and M. I. Mishchenko (2004), Calculation of radiative fluxes from the surface to top of atmosphere based on ISCCP and other global data sets: Refinements of the radiative transfer model and the input data, *J. Geophys. Res.*, *109*, D19105, doi:10.1029/2003JD004457.